FISEVIER

Contents lists available at ScienceDirect

Journal of Alloys and Compounds

journal homepage: www.elsevier.com/locate/jalcom



Research Article

Novel bioactive Ti-Zn alloys with high strength and low modulus for biomedical applications



M.H. Qi ^a, J.L. Xu ^{a,*}, T. Lai ^a, J. Huang ^a, Y.C. Ma ^a, J.M. Luo ^a, Y.F. Zheng ^{b,*}

- ^a School of Materials Science and Engineering, Nanchang Hangkong University, Nanchang 330063, PR China
- ^b School of Materials Science and Engineering, Peking University, Beijing 10087, PR China

ARTICLE INFO

Article history: Received 15 August 2022 Received in revised form 23 September 2022 Accepted 10 October 2022 Available online 13 October 2022

Keywords: Ti-Zn alloy Hot-press sintering Mechanical properties Cytocompatibility Biomedical application

ABSTRACT

To address new challenges in current biomedical titanium alloys, novel binary Ti-Zn alloys with high strength, low elastic modulus, excellent corrosion resistance, and intrinsic bioactivity, were prepared via hot-press sintering. In this paper, the microstructure, mechanical properties, corrosion behaviors, and in vitro biological properties of the Ti-Zn alloys were systematically investigated. The Ti-Zn alloys mainly consist of α -Ti and Ti₂Zn phases, in which the Ti₂Zn phase plays a good role in precipitation strengthening, and the number gradually increases with increasing the Zn contents. All of the compressive strength, elastic modulus, and nanohardness of the Ti-Zn alloys increase first, and then decrease with increasing the Zn contents. The Ti-Zn alloys show great corrosion resistance with the polarization resistance of more than 10^4 Ω /cm², and the resistance continuously increases with increasing the immersion times in SBF solution. The Ti-Zn alloys possess hydrophilic surfaces with contact angles of approximately $34^\circ \sim 60^\circ$. The concentration of Zn ions released from the Ti-20Zn alloy in 0.9% NaCl solution is much lower than that of the biosafety intake. The Ti-Zn alloys exhibit favorable cytocompatibility, which are very beneficial to the spread, proliferation, and differentiation of the MC3T3-E1 cells. The above-mentioned results suggest the Ti-Zn alloys can be promising candidates for biomedical applications.

© 2022 Elsevier B.V. All rights reserved.

1. Introduction

Titanium and its alloys have been widely used in the field of orthopedic and dental implants due to their great corrosion resistance, good mechanical strength, admirable biocompatibility, and MRI compatibility [1–4]. However, their high elastic modulus (~110 GPa) and biological inertness remain major concerns, resulting in "stress shielding effect" [5,6] and poor bone-implant bonding [7,8], respectively, eventually failure of implantations. In addition, clinically used Ti-6Al-4V alloy has the problem of releasing toxic V and Al ions [9,10], while pure Ti exhibits unsatisfactory mechanical and wear properties, and its wear products can cause "particle disease" [11]. Therefore, it is urgent to develop novel titanium alloys with high strength, low modulus, and intrinsic bioactivity by adding non-toxic alloying elements. In recent years, various binary titanium alloys have been designed by adding alloying elements, such as Nb, Mo, Mn, Fe, Cu, and Mg, etc. [12-19]. Nonetheless, among the novel titanium alloys, each has its advantages and disadvantages. For

example, Ti-Mo alloys showing excellent integrated mechanical properties are bioinert [13], Ti-Cu alloys with nice antibacterial properties exhibit high elastic modulus [16], while Ti-Mg alloys possess matching modulus and bioactivity, but the Mg in the Ti-Mg alloys degrades too fast and produces hydrogen [17].

Currently, metallic Zn has aroused people's interest as a biodegradable metal for its fascinating characteristics. One, Zn has a slower degradation rate than Mg without hydrogen produced during the degradation [20-22]. Liu et al. [21] studied the in vitro degradation behavior of pure zinc in different solutions and found that the pure Zn had a relatively moderate corrosion rate. Bowen et al. [22] implanted pure zinc wires into the abdominal aorta of rats, which identified that the biodegradable zinc had ideal biocorrosion behavior. Two, Zn exhibits acceptable biocompatibility [23,24]. Yang et al. [23] investigated the in vivo degradation behavior of pure Zn scaffolds in a rabbit abdominal aorta model, and the results showed that the Zn scaffolds had good biocompatibility without severe inflammation, platelet aggregation, thrombosis, and intimal hyperplasia. Guo et al. [24] studied the in vitro performance of pure zinc wires, which showed favorable cytocompatibility and partly antibacterial effect on S. aureus and E. coli. Three, Zn possesses excellent osteogenic ability [25,26]. Guo et al. [25] prepared pure zinc as

^{*} Corresponding authors.

E-mail addresses: jlxu@nchu.edu.cn (J.L. Xu), yfzheng@pku.edu.cn (Y.F. Zheng).

membrane material for guided bone regeneration (GBR), demonstrating the favorable osteogenic capability of pure zinc membrane with 300 µm pores in vivo. Four, Zn is also an essential trace element, with recommended daily value of 2 mg/day, which can participate in various physiological activities [27].

Nevertheless, pure Zn as a biomedical material is still confronting some challenges, such as low yield strength (~29.3 MPa), poor ductility (\sim 1.2%) [28], and biotoxicity at a high degradation rate [29]. Considering the excellent biological functionalities and limited cytotoxicity of the metallic Zn, it seems great to combine the mechanical properties of titanium and the bioactivity of zinc. On the one hand, Zn as an alloying element can not only strengthen the mechanical properties through precipitation strengthening effect of titanium zinc intermetallic compound [30], but also enhances the bioactivity by releasing Zn ions in body fluids [25,26]. On the other hand, Zn as a cheap element shows better cost control in actual production compared with the elements of Zr, Nb, Mo, and Ta, etc. [31–33]. Particularly, due to the high saturated vapor pressure of Zn and the large difference in melting point between Ti and Zn, hotpress sintering is an ideal method to prepare the Ti-Zn alloys. To date, to the best of our knowledge, there are no reports about biomedical Ti-Zn alloys. In this paper, novel low-cost bioactive Ti-Zn alloys with nominal compositions of 5, 10, 20, and 30 wt% Zn for permanently implanted application were prepared via hot-press sintering. The microstructure, mechanical properties, corrosion resistance, and in vitro biological properties of the Ti-Zn alloys were systematically investigated, expecting them to be promising candidates for biomedical applications.

2. Experimental procedure

2.1. Preparation of the Ti-Zn alloys

Commercially available Ti powder (purity > 99.7%, -325 mesh) and Zn (purity > 99.7%, -1000 mesh) spherical-like powder, purchased from Beijing Xingrongyuan Technology Co. LTD, China, were used as the raw powders. The Ti-Zn mixed powders were blended using a planetary ball mill (QM-1SP4, Nanjing University Instrument Plant, China) at the speed of 250 r/min for 3 h, and then put into a graphite mold with the diameter of 15 mm. The samples were sintered under 30 MPa pressure in a vacuum hot-press sintering furnace (RYL-25–19, Nanjing Boyuntong Instrument Technology Co. LTD., China) at 800 °C for 30 min and cooled to room temperature in the furnace. The nominal weight percentage of Zn in Ti-Zn alloy was 5%, 10%, 20%, and 30%, and the sintered samples were denoted as Ti-5Zn, Ti-10Zn, Ti-20Zn, and Ti-30Zn, respectively.

2.2. Microstructural characterization

The Ti-Zn alloys were ground to a 2000 grit surface by silicon carbide papers and then mechanically polished with Cr₂O₃ suspension. A scanning electron microscopy (SEM, FEI Nova Nano SEM450, USA) equipped with energy dispersive X-ray (EDS, Oxford Instruments INCA 6650, England) was employed to characterize the microstructure and chemical composition of the Ti-Zn alloys. The porosities of the Ti-Zn alloys were measured by Archimedes drainage method according to ASTM B962-08. The phase composition was examined by X-ray diffraction (XRD, Bruker D8 FOCUS, Germany) with a Cu K α radiation at a scan rate of 2° /min at room temperature. The volume fractions of the phases were calculated by the integral area of the three most characteristic peaks of the XRD patterns, in which the asymmetrical peaks were separated using the Pearson VII function [34]. The chemical composition and electronic states of the Ti-20Zn alloy were performed by X-ray photoelectron spectroscopy (XPS, Shimadzu Kratos Axis Ultra DLD, Britain) with an Al Kα excitation (150 W, 10 mA, 15 kV). The microstructure of Ti20Zn alloy was further investigated by transmission electron microscopy (TEM, FEI Talos F200X, USA) at an acceleration voltage of 200 kV.

2.3. Mechanical property test

Cylindrical samples with the dimension of $\Phi 3 \times 6$ mm were longitudinally cut from the sintered Ti-Zn alloys for compression tests (ASTM-E9–09), and an electronic universal testing machine (WDW-50, Jinan Shijin group Co. LTD, China) was used with a strain rate of 0.1 mm/min under room temperature. The elastic modulus was determined according to the ASTM E111–97 [35] from the stress-strain curves. For each alloy, three duplicate samples were measured and averaged.

The elastic modulus and indentation nanohardness of the Ti-Zn alloys were measured using a nanoindentation tester (TTX-NHT3, Anton Paar, Austria) with Berkovich indenter (maximum load: 450 mN, loading time: 60 s, pause: 30 s, and unload time: 60 s) according to ISO 14577–1 [36].

2.4. Electrochemical measurement

The electrochemical measurement of the Ti-Zn alloys was performed on an electrochemical working station (CHI650D, Shanghai Chenhua instrument Co. LTD, China) in the SBF solution [37] under room temperature. A conventional three-electrode system was employed, which was equipped with a platinum foil electrode as the auxiliary electrode, a saturated calomel electrode (SCE) as the reference electrode, and the samples with the exposed area of 1 cm² as the working electrodes. Before other tests, the open-circuit potential (OCP) was performed for 1800 s to reach a steady state. Electrochemical impedance spectroscopy (EIS) was conducted with the amplitude of 10 mV in a frequency from 10⁵ Hz to 10⁻² Hz and fitted by the software of ZsimpWin. Potentiodynamic polarization curves were obtained over a potential ranged from - 0.8-1.0 V at a scan rate of 1 mV/s. The corrosion potential (E_{corr}) and corrosion current density (I_{corr}) were interpolated by linear fitting and Tafel extrapolation. The long-term electrochemical corrosion behavior of the Ti-20Zn alloy immersed in the SBF solution for 28 days was also investigated by EIS.

2.5. Immersion test

The Ti-20Zn alloy was immersed in the 0.9% NaCl solution at 37 °C \pm 0.5 °C for 28 days with a solution-to-area ratio of 1.14 cm²/mL (ASTM-G31–72). The dimension of the sample was $\Phi11\times1$ mm, and the volume of the immersion solution was 2 mL. The concentrations of Zn ions in the solution were measured by flame atomic absorption spectrophotometer (AAS NovAA800, Analytik Jena, Germany). The experiment was repeated three times for each group.

2.6. Water contact angle test

The water contact angles of the Ti-Zn alloys were determined by an optical contact angle tester (DSA 100, Kruss, Germany) with a 5 μL water droplet, and the biomedical Ti-6Al-4 V alloy (TC4, Xi 'an Saite Metal Material Development Co. LTD, China) was used as the control. Before the test, the samples were ground to a 2000 grit surface, and each sample was tested three times in different places.

2.7. Cytocompatibility test

The cytotoxicity was tested by direct seeding on the surfaces of the Ti-Zn alloys according to ISO 10993–5: 2009, the TC4 alloy as the control. The effect of the Ti-Zn alloys on the cell viability of mouse

embryonic osteoblast precursor cells (MC3T3-E1 cells) was detected by the CCK-8 assay (Dojindo Lab, Japan), and the negative control group involved cell culture medium was set up. Each group of materials was placed in 48-well plates, and 1 mL cell suspension (1 $\times 10^4$ MC3T3-E1 cells) was inoculated into each well plate, and cultured in an incubator at 37 °C with 5% CO2 for 1, 4, and 7 days. The supernatant was sucked out and replaced with 1 mL fresh culture medium and 0.1 mL CCK-8 solution. The solution was cultured in humidified atmosphere incubator with 5% CO2 at 37 °C for 2 h. The solution was sucked out and transferred to a 96-well plate. The absorbance (OD) value was measured at 450 nm using a microplate reader (Multiskan Spectrum, Thermo Scientific, USA).

To observe the morphologies of the cells, the MC3T3-E1 cells was also seeded on the Ti-Zn alloys and TC4 alloy, and incubated for 1 day and 7 days, respectively. And then the incubated samples was covered in 2.5% glutaraldehyde solution for 1 h and then washed in phosphate buffered saline (PBS) and distilled water. Subsequently, the samples were continuously dehydrated in different concentrations of alcohol, and then dried in the air. Finally, the samples was sprayed with gold and observed by the SEM.

2.8. ALP activity test

The ALP activity of the MC3T3-E1 cells was tested after being cultured on the Ti-Zn alloys for 7 and 14 days, the TC4 alloy as control. After seeding on the surface of the Ti-Zn alloys and the TC4 alloy at different times, MC3T3-E1 cells were rinsed with PBS two times and lysed with 200 μm 0.2% Triton X-100 on ice for 15 min. The total intracellular protein content was examined by a BCA protein assay kit and measured using a microplate reader at 562 nm. The ALP activity (expressed as μmol of converted p-nitrophenol/min) with p-nitrophenyl phosphate as the substrate of the MC3T3-E1 cells was evaluated at 405 nm using the microplate reader and normalized by the total intracellular protein contents.

3. Results and discussion

3.1. Microstructural analysis of the Ti-Zn alloys

Fig. 1 shows the SEM backscattered electron (BSE) images and porosities of the Ti-Zn alloys with different Zn contents. The surface of the samples is mainly composed of white, gray, and black three regions. The white island-like regions should be secondary phase precipitates, the black regions are mainly the residual pores volatilized by Zn, and the gray regions are attributed to the Ti matrix. With increasing the Zn contents, the number of while regions gradually increases, and finally coalesces into larger blocks around grain boundaries as shown in Fig. 1(d), which will separate the α -Ti matrix and lead to the brittleness of the Ti-30Zn alloy. According to the EDS spectra shown in Fig. 1(e), the white secondary phase consists of Ti and Zn elements with an atomic ratio of approximately 2: 1, which may be attributed to the Ti₂Zn phase. Zn is known as a beta Ti stabilized element [38]. α -Ti is transformed into β -Ti by isomerization at high temperature and then the Zn is dissolved into β -Ti to form a solid solution. Due to the "active" eutectoid reaction $\beta \rightarrow \alpha$ + Ti₂Zn [30] during the furnace cooling process, the Zn is precipitated outside the grain boundary, resulting in the enrichment of Zn [30]. At the same time, the Ti₂Zn phases nucleate and grow along the grain boundaries. Therefore, the white island-like secondary phase precipitates can be identified as Ti₂Zn. The contents of Zn element in the Ti-Zn alloys obtained by EDS are listed in Table 1. Most of Zn is retained in the Ti-Zn alloys, while a small amount of Zn is volatilized during the sintering process. With increasing the Zn contents, the volatile content of Zn increases, which leads to the formation of more pores in the Ti-Zn alloys. This is also confirmed by the porosity results of Ti-Zn alloys, shown in Fig. 1(f). With increasing the Zn contents, the porosities nearly linearly increase from 6.9 ± 1.1% for Ti-5Zn alloy to 30.4 \pm 2.5% for Ti-30Zn alloy. The increase of porosity should have a great influence on the mechanical properties, corrosion resistance and wettability of the alloys.

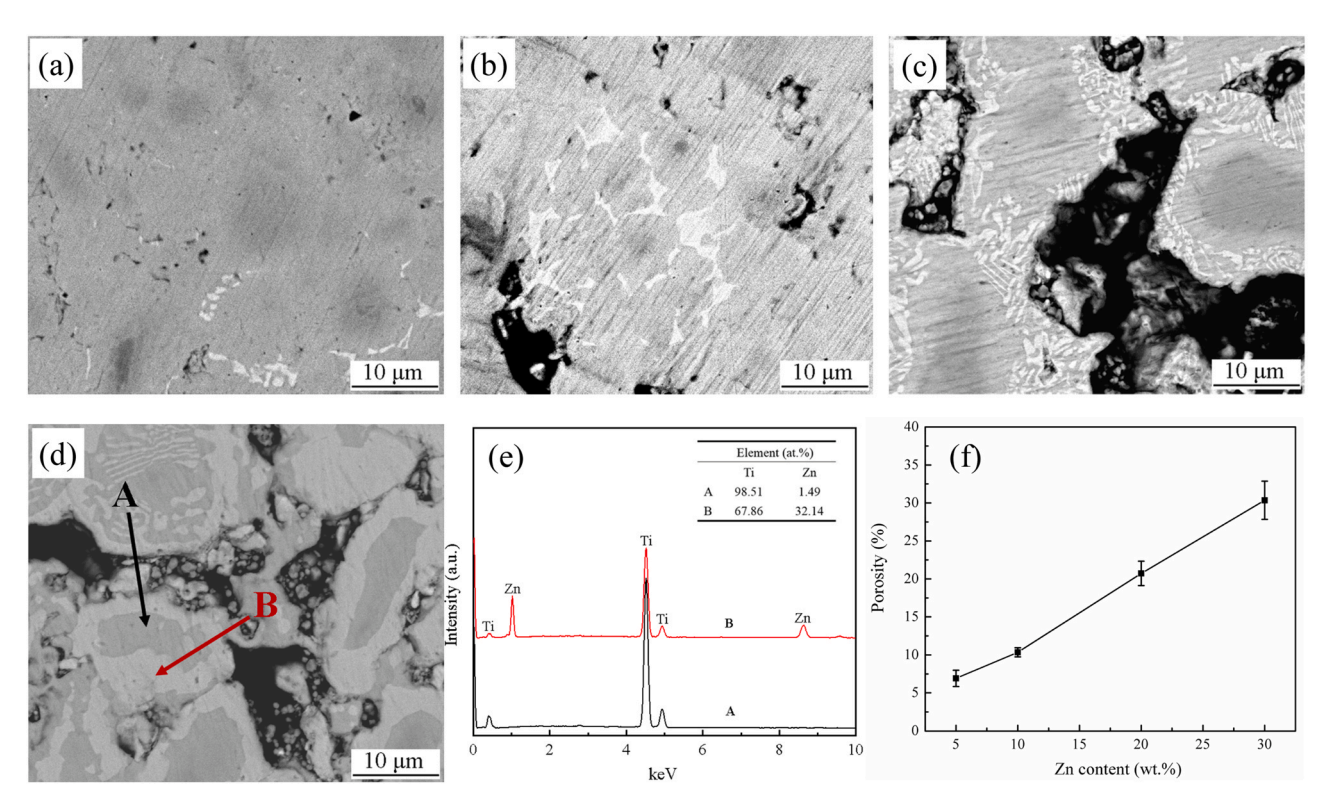


Fig. 1. Surface morphologies and porosities of the Ti-Zn alloys with different Zn contents: (a) 5 wt%; (b) 10 wt%; (c) 20 wt%; (d) 30 wt%; (e) EDS patterns of A and B points in Ti-30Zn alloy; (f) porosities.

Table 1Nominal and actual contents of Zn element in the Ti-Zn alloys.

Sample	Nominal content (wt%)	Actual content (wt%)	Volatile content (wt%)
Ti-5Zn	5	4.63	0.37
Ti-10Zn	10	9.70	0.3
Ti-20Zn	20	18.63	1.37
Ti-30Zn	30	27.97	2.03

Fig. 2(a) shows the XRD patterns of the Ti-Zn alloys with different Zn contents. The Ti-Zn alloys are mainly compose of α -Ti phase and Ti₂Zn phase, and the intensity of the Ti₂Zn diffraction peaks increases, while the intensity of α -Ti diffraction peak decreases with increasing the Zn contents. Especially, when the Zn content reaches 30 wt%, the intensity of the Ti₂Zn diffraction peak is much higher than that of α -Ti phase, indicating that the Ti₂Zn phase becomes the dominant phase and the number of Ti₂Zn phase is higher than that of α -Ti phase. The diffraction peaks of the α -Ti phase are clearly found in all of the samples, while almost no obvious diffraction peaks of the Ti₂Zn phase can be observed when the Zn content is lower than 10 wt%. Herein, the overlap peaks are separated into α -Ti and Ti₂Zn peaks by the Pearson VII function [34], and the volume fractions of the alloy phases were estimated by the reference intensity ratio method (RIR) [39,40]. The volume fractions of α -Ti and Ti₂Zn in the Ti-Zn alloys derived from XRD patterns is shown in Fig. 2(b). The fractions of the α -Ti phase rapidly decreases from 93.61% for Ti-5Zn alloy to 38.18% for Ti-30Zn alloy with increasing the Zn contents, while the Ti₂Zn phase correspondingly increases from 6.39% for Ti-5Zn alloy to 61.82% for Ti-30Zn alloy. This result is greatly consistent with the Fig. 1. In addition, the diffraction patterns of the Ti-5Zn and Ti-10Zn alloys show that the strongest diffraction peak of α -Ti phase changes from $2\theta = 40.3^{\circ}$ to $2\theta = 38.5^{\circ}$, which may be attributed to the preferred orientation caused by residual stress during the hot-press sintering process.

To further investigate the microstructure of the Ti-Zn alloys, the TEM images of the Ti-20Zn alloy are shown in Fig. 3. It can be seen from TEM bright field image (Fig. 3(a)) that some long crank-shaped and pebble-shaped gray precipitates with the grain sizes ranged from 0.5 to $2\,\mu m$ are randomly dispersed in the relatively bright white $\alpha\textsc{-Ti}$ matrix, in which it also contains a high density of dislocations pile-up and tangles. The EDS spectra (Fig. 3(b)) reveal that the precipitates are mainly composed of the Ti and Zn elements with an atomic ratio of approximately 2:1. Moreover, the precipitates are identified as Ti_2Zn phases with tetragonal structure by the high-resolution transmission electron microscopy (HRTEM) images and

selected area electron diffraction (SEAD) pattern shown in Fig. 3(d), and the rest are $\alpha\textsc{-Ti}$ matrix (Fig. 3(c)). The crystal band axis and PDF card corresponding to the diffraction pattern of Ti $_2$ Zn phase is [1–10] and 04–004–3986, respectively, while the $\alpha\textsc{-Ti}$ matrix is [1–100] and 00–044–1294. The HAADF image and elemental mapping of the Ti-20Zn shown in Fig. 3(e) further illustrate the morphology and distribution of the Ti $_2$ Zn precipitated phase in the Ti-20Zn alloy. Moreover, the high density dislocations distributed over the Ti-20Zn alloy may be attributed to the uniaxial compression during the sintering process. The movement of dislocations is hindered by dispersedly distributed secondary phases and form the dislocations pile-up and tangles, which can greatly strengthen the mechanical strength of the alloy.

XPS broad scan and high-resolution spectra of the Ti-20Zn alloy are shown in Fig. 4. From Fig. 4(a), the C 1 s, Ti 2p, O 1 s, Zn 2p, and Zn LMM are mainly observed, in which the C element is from the atmospheric contamination, indicating that the surface of the Ti-20Zn alloy is mainly composed of Ti, Zn, and O elements. The highresolution spectrum of O 1 s shows three peaks located at 532.6 eV, 531.3 eV, and 529.9 eV, corresponding to the binding energies of H₂O, Ti-OH, and Ti-O, respectively [41]. The chemical absorbed hydroxyl groups can be contributed to the hydrophilicity of the alloy and effectively promote the cell adhesion and growth on the surface. Four peaks are observed from the high-resolution spectrum of Ti 2p at the binding energies of 464.0 eV, 458.3 eV, 456.4 eV, and 453.2 eV, respectively. The expected doublet with Ti $2p_{3/2}$ at 458.3 eV and Ti $2p_{1/2}$ at 464.0 eV is assigned to the Ti^{4+} of TiO_2 [42,43], the 456.4 eV corresponds to the Ti³⁺ of Ti₂O₃, and the 453.2 eV belongs to the metallic Ti⁰ [43]. The peaks of Zn 2p located at 1021.7 eV and 1044.8 eV are characteristic for the sphalerite ZnO [44]. However, the binding energy of metallic Zn is very close to that of ZnO and hard to identify, while the Auger electron energy spectrum is more distinguishable [45]. Two Auger electron peaks of the Zn at 497.9 eV and 493.3 eV can be detected, which is assigned to ZnO and Ti₂Zn [46,47], respectively. Therefore, according to the XPS analysis results, the surface of the Ti-20Zn alloy is mainly composed of TiO₂, ZnO, and Ti₂Zn, as well as amounts of chemically absorbed hydroxyl groups.

3.2. Mechanical properties of the Ti-Zn alloys

Fig. 5 shows the typical compressive stress-strain curves of the Ti-Zn alloys with different Zn contents, and the mechanical properties extracted from the curves are listed in Table 2. All of the stress-strain curves contain the elastic, plastic, and parabola stages [48]. All of the compressive strength, yield strength and elastic modulus of

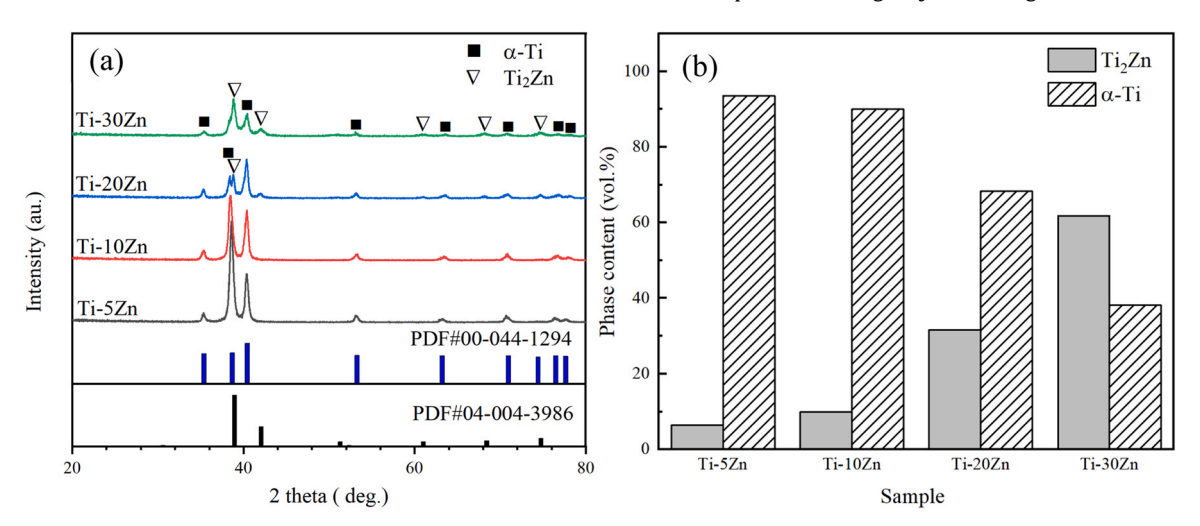


Fig. 2. XRD patterns of the Ti-Zn alloys prepared with different Zn contents (a) and the volume ratio of α -Ti and Ti₂Zn phases in the Ti-Zn alloys (b).

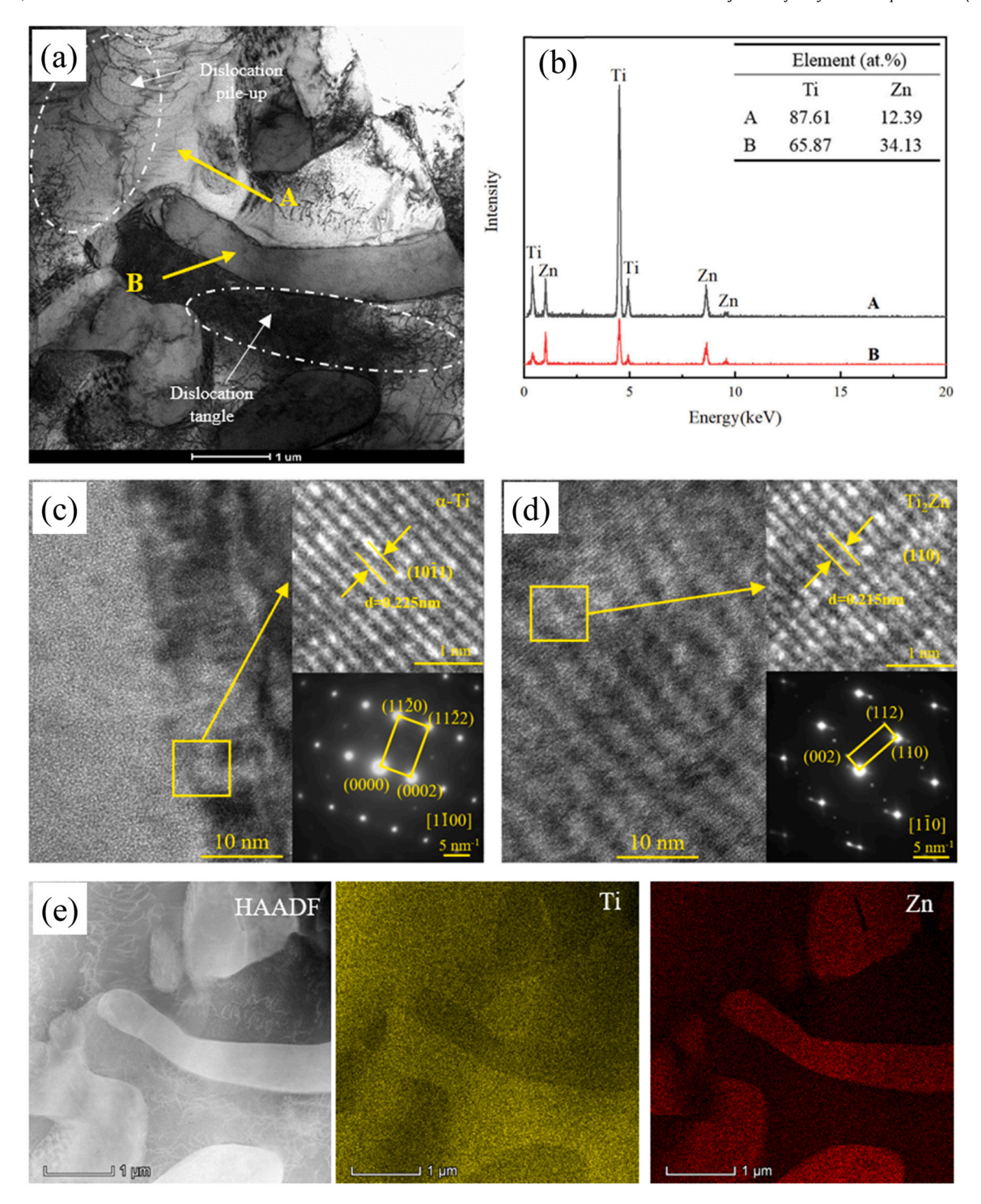


Fig. 3. TEM images of the Ti-20Zn alloy: (a) bright field image; (b) EDS spectra of A and B points; (c) HRTEM and SEAD images of point A; (d) HRTEM and SEAD images of point B; (e) HAADF and elemental mapping images.

the Ti-Zn alloys increase first, and then decrease with increasing the Zn contents. The addition of Zn alloying element greatly strengthens the mechanical properties because the diffusely distributed ${\rm Ti}_2{\rm Zn}$ phases along the grain boundaries play the role of precipitation strengthening. However, the excessive Zn content leads to the formation of more micropores and higher porosities (seen in Fig. 1 and Fig. 6) as well as the increase of the excessive ${\rm Ti}_2{\rm Zn}$ precipitates, all of which will result in the occurrence of stress concentration and deteriorate the strength of the Ti-Zn alloys finally. Especially, the rapid decrease of compressive strength of Ti-30Zn alloy is due to the

fact that the content of Ti_2Zn in the alloy is higher than that of the Ti matrix (seen in Fig. 2b), which destroys the continuity of the α -Ti and makes the brittleness of the Ti-30Zn alloys increase sharply. This can be verified by the fracture morphologies of Ti-20Zn and Ti-30Zn alloys, shown in Fig. 6. Some dimples and cleavage facets with a few pores can be observed on the fracture surface of Ti-20Zn alloy, while there are many pores and intergranular fractures on the Ti-30Zn alloy. The fracture morphologies show that the Ti-20Zn alloy possesses much more ductile behavior than Ti-30Zn alloy, which is in good agreement with the compressive properties. Nevertheless, the

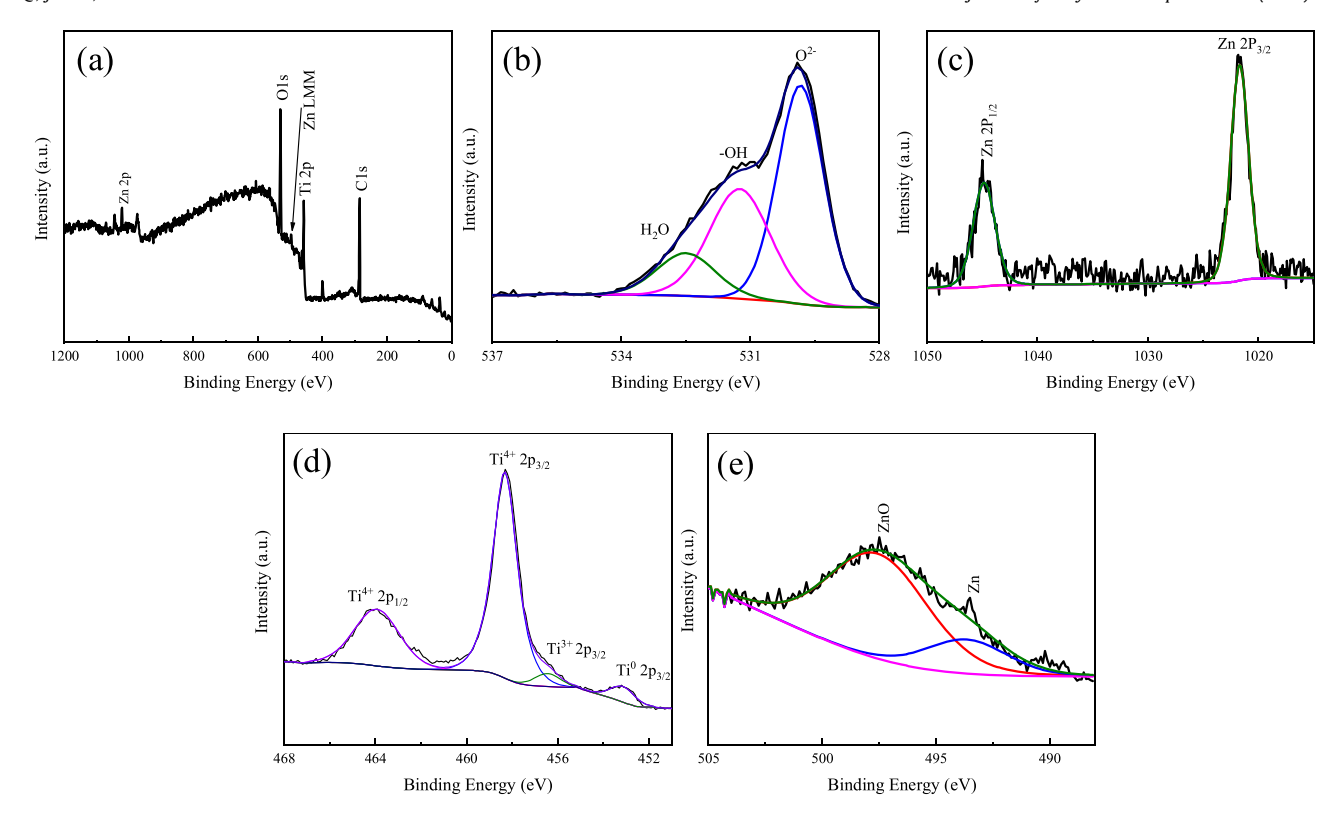


Fig. 4. XPS broad scan spectrum (a) and high-resolution spectra of O 1 s (b), Zn 2p (c), Ti 2p (d), and Zn LMM (e) of the Ti-20Zn alloy.

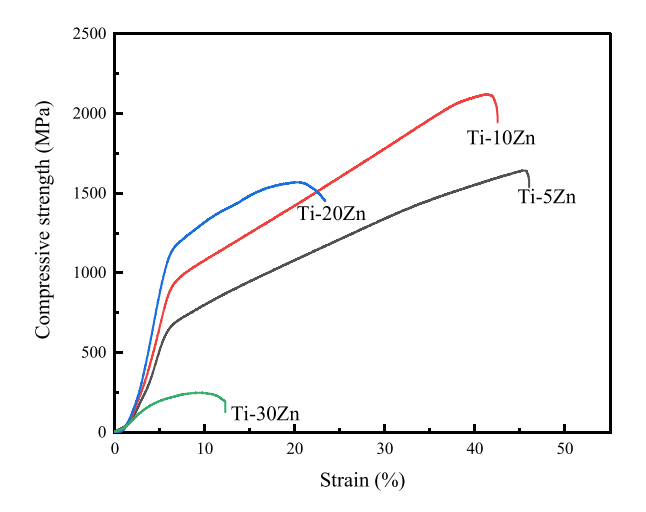


Fig. 5. Typical compressive stress-strain curves of Ti-Zn alloys with different Zn contents.

compressive strength of the Ti-Zn alloys is much higher than that of the human bone [49] and also higher than the TC4 alloys of \sim 770 MPa [50]. The elastic modulus of the Ti-Zn alloys is ranged from 16.6 to 26.8 GPa, very close to the human bone (\sim 21 GPa) [49], and is much lower than those of the alloys reported in the literature

[51]. This result suggests that the Ti-Zn alloys have excellent mechanical properties for biomedical applications.

To eliminate the "stress shielding effect" and prolong the service time, implant materials are required high strength and low modulus, thus the ratio of strength to modulus is frequently used to evaluate the materials [40,52]. As shown in Fig. 7, the ratios of 20% compressive strength to elastic modulus are 6.57%, 6.87%, and 5.73% for Ti-5Zn, Ti-10Zn, and Ti-20Zn, respectively, which is much higher than the CP-Ti of 0.43% [53,54] and those of the Ti-xNb alloys [54]. The low modulus of the Ti-Zn alloys is mainly attributed to the micropores formed by the volatilization of Zn during the sintering process, and their superior strength is attributed to the precipitation strengthening effect of the Ti₂Zn phases. Besides, the elastic energies (W_e) shown in Table 2 are calculated by the following formula [55]:

$$W_e = \varepsilon_e \times \sigma_y / 2$$

where the ε_e and σ_y stands for the elastic strain and the yield strength, respectively. The elastic energies of the Ti-Zn alloys can be ranged from 19.81 to 36.07 MJ/m³, which is much higher than the TC4 alloy of ~3 MJ/m³ and the Ti-Cu alloy of 9 MJ/m³ [56]. This result indicates the Ti-Zn alloys have an excellent self-recovery ability to serve as hard tissue replacement.

Fig. 8(a) shows the typical loading-unloading nanoindentation curves of the Ti-Zn alloys and the average values of elastic modulus and nanohardness are shown in Fig. 8(b). With increasing the Zn

Table 2Mechanical properties of the Ti-Zn alloys with different Zn contents and CP-Ti.

Sample	Compressive strength /MPa	Yield strength /MPa	20% Compression strength /MPa	Elastic modulus /GPa	Elastic energy /MJ·m ⁻³
Ti-5Zn	1476 ± 150	651 ± 3	1091 ± 18	16.6 ± 1.4	19.81
Ti-10Zn	1906 ± 215	934 ± 32	1394 ± 26	20.3 ± 1.4	30.95
Ti-20Zn	1538 ± 43	1136 ± 10	1536 ± 45	26.8 ± 1.8	36.07
Ti-30Zn	225 ± 22	-	=	4.3 ± 0.8	_
CP-Ti[53,54]	-	-	450	105	-

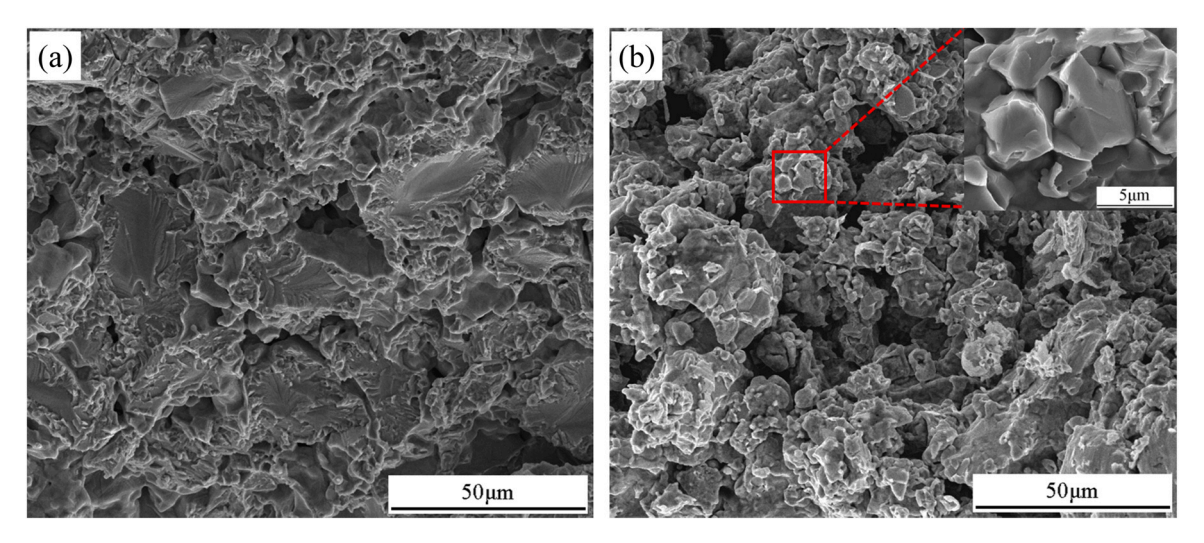
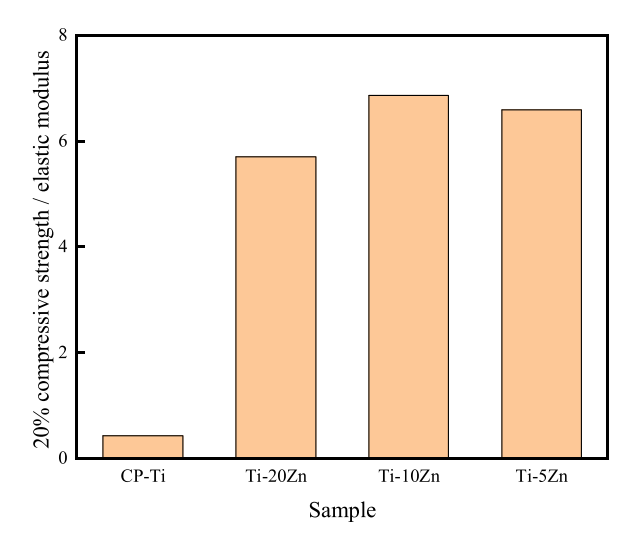


Fig. 6. Fracture morphologies of the Ti-20Zn alloy (a) and Ti-30Zn alloy (b).



 $\textbf{Fig. 7.} \ \ \text{Ratios of } 20\% \ compressive \ strength \ to \ elastic \ modulus \ for \ the \ Ti-Zn \ alloys \ and \ CP-Ti.$

contents, the elastic modulus increases from 51.21 \pm 2.32 GPa for Ti-5Zn alloy to 143.77 \pm 6.85 GPa for Ti-20Zn alloy, reaching the maximum value, and then decreases to 133.06 \pm 15.11 GPa for Ti-30Zn alloy. This variation trend is greatly consistent with the results of compression tests. However, the elastic modulus values obtained by

the two methods are quite different indeed. According to the research of Doerner and Nix [57], the elastic modulus obtained by nanoindentation test is larger than the real value of the materials. Besides, the elastic modulus obtained by the nanoindentation is more microscopic and less affected by the micropores, while the elastic modulus obtained by the compression is more macroscopic and greatly affected by the micropores. Thus, the elastic modulus of the nanocompression test is much larger than that of the compression test. The nanohardness of the Ti-Zn alloys shows the similar trend to the elastic modulus, and it increases from 157.51 ± 18.34 HV for Ti-5Zn to 390.18 ± 42.84 HV of Ti-20Zn, reaching the highest nanohardness, and then decreases to 269.69 ± 34.60 HV for Ti-30Zn with increasing the Zn contents. The increase of the namohardness of Ti-Zn alloys is also mainly attributed to the precipitation strengthening of the Ti₂Zn phases. Moreover, the increase of hardness can also greatly improve the wear resistance of the Ti-Zn alloys and make them more conducive to become a hard tissue replacement [11,58].

3.3. Corrosion behavior of the Ti-Zn alloys

Fig. 9 depicts the potentiodynamic polarization curves of the Ti-Zn alloys in the SBF solution at room temperature, and the electrochemical parameters of corrosion potential ($E_{\rm corr}$), corrosion current density ($I_{\rm corr}$), anodic and cathodic Tafel slope ($\beta_{\rm a}$ and $\beta_{\rm c}$), and polarization resistance ($R_{\rm p}$) obtained by the Tafel region extrapolation are summarized in Table 3. The Ti-Zn alloys exhibit excellent

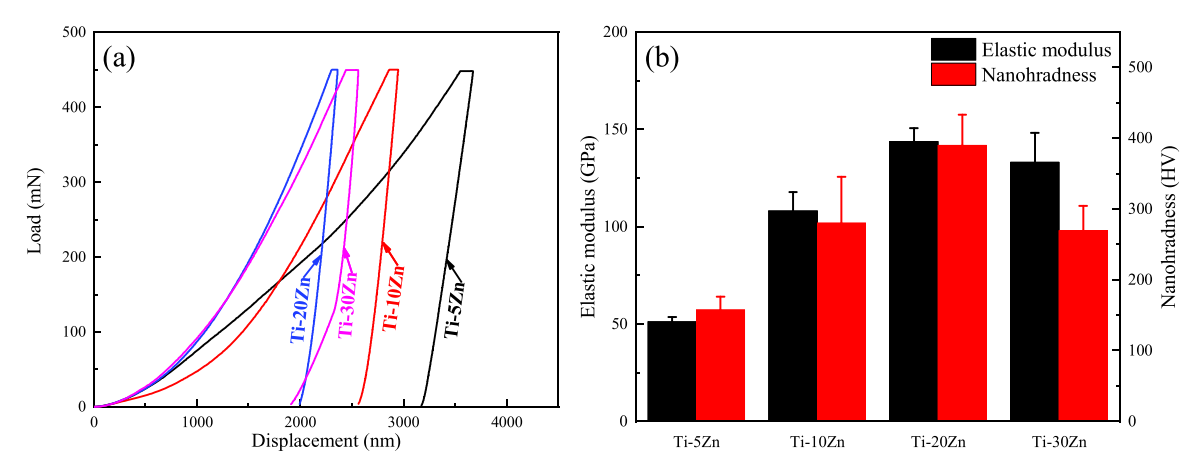


Fig. 8. Typical loading-unloading nanoindentation curves (a) and elastic modulus and nanohardness (b) of the Ti-Zn alloys with different Zn contents.

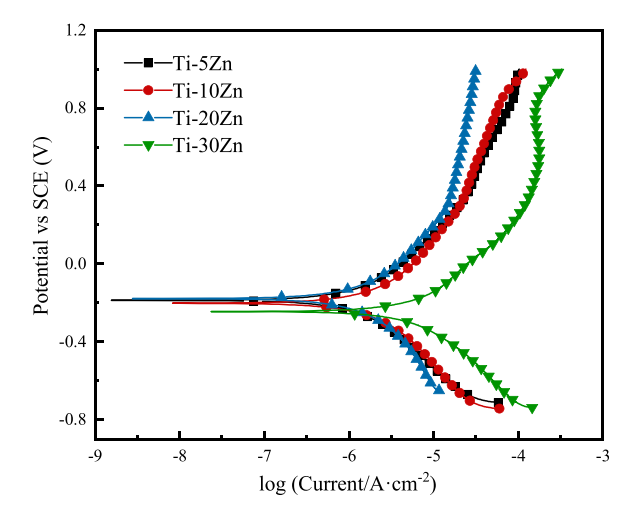


Fig. 9. Potentiodynamic polarization curves of Ti-Zn alloys with different Zn contents.

Table 3Corrosion parameters of polarization curves of Ti-Zn alloys with different Zn contents.

Sample	E _{corr} /V	I _{corr} / (A/cm ²)	β _a (V/dec)	β _c (V/dec)	$R_{\rm p}~(\Omega/{\rm cm}^2)$
Ti-5Zn	-0.187 -0.202	6.925 × 10 ⁻⁷ 9.753 × 10 ⁻⁷	0.165	0.170	52631
Ti-10Zn Ti-20Zn	-0.202 -0.178	7.415 × 10 ⁻⁷	0.170 0.170	0.171 0.173	38035 50266
Ti-30Zn	-0.245	3.631×10^{-6}	0.172	0.180	10526

corrosion resistance and no pitting corrosion can be found in the curves. The polarization curves of the Ti-Zn alloys present the similar forms and characteristics in both cathodic and anodic branches, indicating that the Zn contents have little effect on the corrosion behavior of the Ti-Zn alloys. This result is further illustrated by the almost identical values for β_a and β_c of the Ti-Zn alloys. As the Zn content is equal to or below 20 wt%, the corrosion current density of the Ti-Zn alloys is at the level of 10^{-7} A/cm². However, when the Zn content increases to 30 wt%, the corrosion current density of Ti-Zn alloy increases to 10^{-6} A/cm², indicating that the corrosion resistance of the Ti-30Zn alloy significantly decreases. This is mainly because the Ti-30Zn alloy has more micropores, higher porosity and more Ti₂Zn phases, resulting in larger real contact area and more galvanic corrosion, respectively. All of the polarization resistance of the Ti-Zn alloys is more than $10^4 \Omega/\text{cm}^2$, which is attributed to the titanium oxide passivation film formed on the surface (seen in Fig. 4d), similar to the reported Ti-Ta alloy [59] and Ti-Cu alloy [60]. The results show that the Ti-Zn alloys have great corrosion resistance in the SBF solution, which can be potential materials for biomedical applications.

Fig. 10 shows the open-circuit potential (OCP) of the Ti-20Zn alloy immersed in the SBF solution for 28 days. The OCP value shows a rapid increase in the first 4 days, and then keeps a slow increase. The continuous increase of the OCP values illustrates that a passivated oxide film is formed on the surface of the Ti-20Zn alloy, and the oxide film is continuously enhanced, which can greatly enhance the surface thermodynamic stability and decrease the corrosion tendency.

Fig. 11 shows the experimental and fitted electrochemical impedance spectra (EIS) of the Ti-20Zn alloy immersed in the SBF solution for different days at room temperature. The Nyquist plots are characterized by capacitance semicircles, in which the diameters of the semicircles increase with prolonging the immersion times, indicating the corrosion resistance of the Ti-20Zn alloy gradually enhances. All of the Bode plots show one time constant, and its phase angles in the low-frequency region increase with prolonging the immersion times as well, suggesting that the surface corrosion of Ti-20Zn alloy is alleviated. Moreover, the Bode plots present the typical

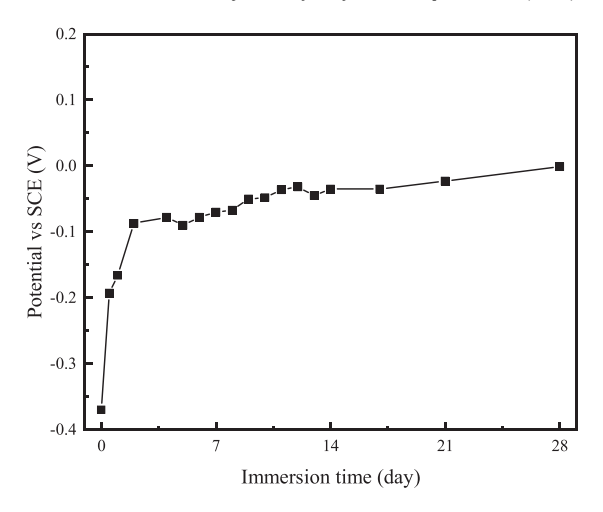


Fig. 10. OCP-time curve of the Ti-20Zn alloy immersed in SBF solution for 28 days.

characteristics of a thin passivation film formed on the metal surface [61,62]. Therefore, the EIS data can be fitted by an equivalent circuit R_s (QR_{ct}), and the fitting parameters are listed in Table 4, in which the R_s , R_{ct} , Q, and n stands for the solution resistance, charge transfer resistance, constant phase element (CPE), and dispersion coefficient of the CPE, respectively. When n = 1, Q represents the pure capacitance; when n = 0, Q is the pure resistance; when 0 < n < 1, n represents the roughness of the working electrode [63,64].

As disclosed from Table 4, all of the Chi-square values are within 10^{-3} during the fitting process, further confirming that the equivalent circuit is appropriate. The Ti-20Zn alloy exhibits excellent corrosion resistance, being attributed to the continuous formation of the passivation film on the surface during the immersion process. With prolonging the immersion times, the $R_{\rm ct}$ values of Ti-20Zn alloy increase continuously, indicating that the resistance of the passivation film is getting larger and the passivation effect is getting better, which can improve the corrosion resistance of the Ti-20Zn alloy. At the same time, the n values of Ti-20Zn alloy slightly increase with prolonging the immersion times, which indicates that the roughness of the passivation film decreases gradually and becomes more smooth and dense. This is beneficial to improve the corrosion resistance of the alloy. The EIS results of the Ti-20Zn alloy are greatly consistent with the results of the OCP.

3.4. Biological analysis of the Ti-Zn alloys

In order to evaluate the wettability of the Ti-Zn alloys, the water contact angles were measured, shown in Fig. 12, the TC4 alloy as the control. The contact angles of the Ti-Zn alloys gradually decrease from 60.05° for Ti-5Zn alloy to 34.96° for Ti-30Zn. All of the contact angles of the Ti-Zn alloys are lower than 65°, illustrating that the Ti-Zn alloys belong to the hydrophilic biomaterials [65], which can support mammalian cell attachment and effectively activate plasma coagulation cascades through the mechanism of surface adsorbed proteins [62]. The contact angles of the Ti-Zn alloys are comparable or even lower than those of TC4, Ti-Au, Ti-Mg and Ti-Nb-Mg alloys reported in the literature [66–68]. The better hydrophilicity of Ti-Zn alloys is mainly attributed to the presence of a large amount of adsorbed -OH on the surface (seen in Fig. 4b), which can greatly reduce the contact angle of the alloy. Moreover, some micropores distributed over the surface of the Ti-Zn alloys can increase the surface roughness and reduce the contact angle of the alloys.

The Zn ions release curve of the Ti-20Zn alloy immersed in 0.9% NaCl solution for different times is shown in Fig. 13. The release amount of Zn ions from the Ti-20Zn alloy gradually increases with prolonging the immersion times, and the average daily release

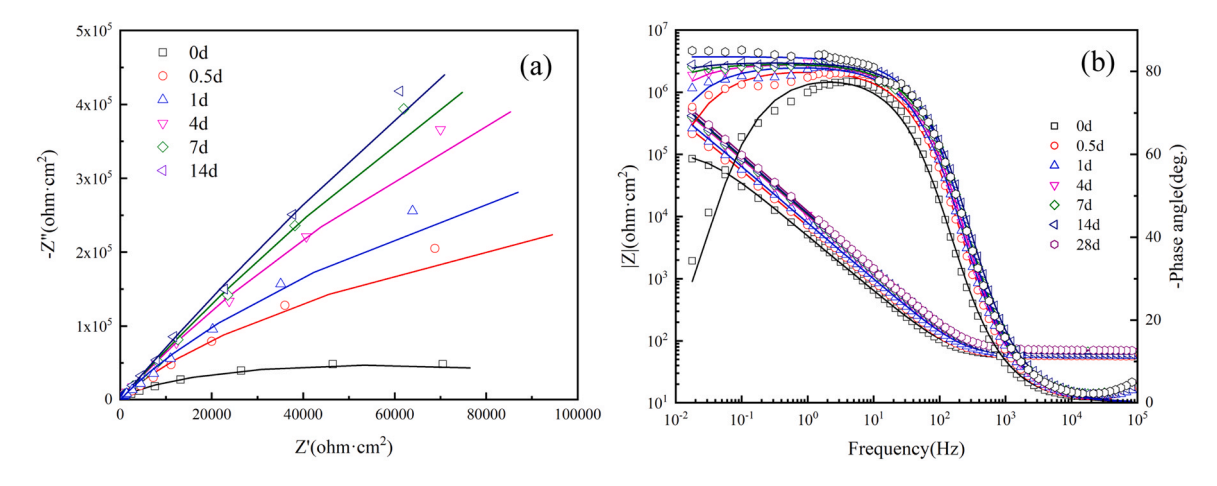


Fig. 11. EIS curves of Ti-20Zn alloy immersed in the SBF solution for different days: (a) Nyquist plot; (b) Bode plot.

 Table 4

 Fitting results of EIS plots of the Ti-20Zn alloy immersed in the SBF solution for different days.

Immersion time	$R_{\rm s}/\Omega\cdot{\rm cm}^2$	$Q_1/S \cdot s^n$	n_1	$R_{\rm ct}/\Omega\cdot{\rm cm}^2$	Chi-square
0	56.53	3.973 × 10 ⁻⁵	0.89	1.117 × 10 ⁵	1.92×10^{-3}
0.5	56.73	2.740×10^{-5}	0.90	1.022×10^{6}	2.28×10^{-3}
1	57.47	2.387×10^{-5}	0.91	1.929×10^{6}	1.56×10^{-3}
4	68.78	1.817×10^{-5}	0.91	5.290×10^{6}	2.39×10^{-3}
7	66.34	1.727×10^{-5}	0.91	1.135×10^{7}	3.92×10^{-3}
14	61.27	1.654×10^{-5}	0.91	1.834×10^{7}	3.73×10^{-3}
28	70.63	1.490×10^{-5}	0.93	9.740×10^{7}	4.12×10^{-3}

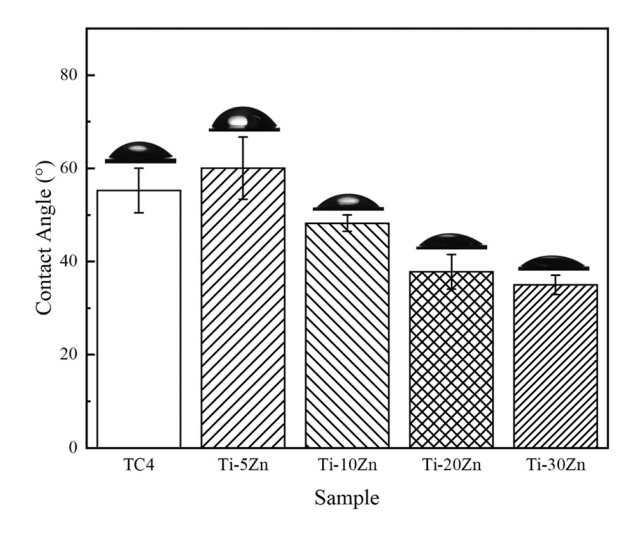


Fig. 12. Water contact angles of the Ti-Zn alloys and TC4 alloy.

amount is approximately 0.156 mg/L (2.4×10^{-6} mol/L), much lower than the biosafety daily release amount of Zn ions (15 mg/L) [69], indicating that the Zn ions release in this condition is very low and safe. According to the study of C. Ning et al. [70], when the concentration of Zn ions was lower than 10^{-4} mol/L, it has no obvious cytotoxicity to fibroblasts. This is since the Zn exists mainly in the form of Ti_2Zn phase in Ti-20Zn alloy, and the TiO_2 passivation film is easily formed on the surface of titanium alloy, which also can greatly inhibit and reduce the release of Zn ions.

To evaluate the cytotoxicity of the Ti-Zn alloys, the in vitro tests of mouse embryo osteoblast precursor (MC3T3-E1) cells were carried out by CCK-8 assay. The optical density (OD) values and cell viabilities of the MC3T3-E1 cells cultured with the Ti-Zn alloys at 1, 4, and 7 days are shown in Fig. 14, the TC4 alloys as the control. All of the OD values increase with increasing the culture times, among

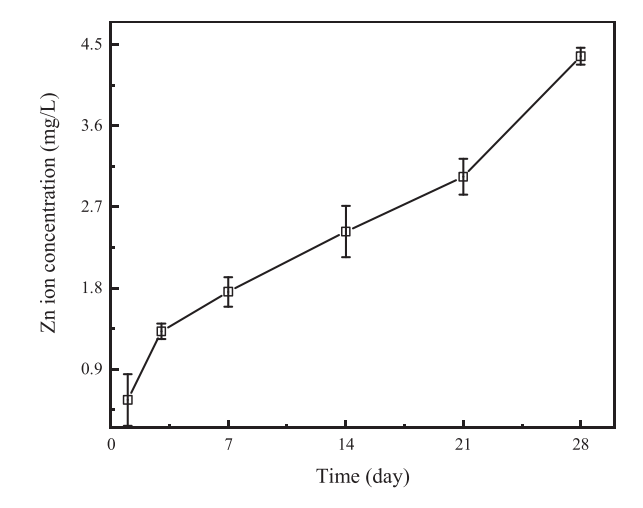


Fig. 13. Zn ions release curve of the Ti-20Zn alloy immersed in 0.9% NaCl solution for different times.

which the OD of the TC4 alloy nearly saturates at 7 days, showing no significant difference with that at 4 days (p > 0.05). The OD values of the Ti-20Zn alloy and Ti-30Zn alloy are significantly higher than those of the TC4 alloy and the negative control (p < 0.01), respectively. Nevertheless, the OD values of Ti-20Zn and Ti-30Zn alloys increase significantly (p < 0.01), reflecting that they can obviously promote cell proliferation. As shown in Fig. 13(b), all of the cell viabilities of the Ti-Zn alloys are higher than 80% after being cultured for different days. Moreover, there is an obvious difference (p < 0.01) in cell viabilities between the negative control and the Ti-20Zn and Ti-30Zn alloys after 1, 4, and 7 days. At the same time, the cell viabilities among the Ti-Zn alloys are also significantly different (p < 0.01). According to the classification standard of cell toxicity [71,72], as the cell viability of the material is higher than 75%, it is considered as a non-cytotoxic material. All of the cell viabilities of

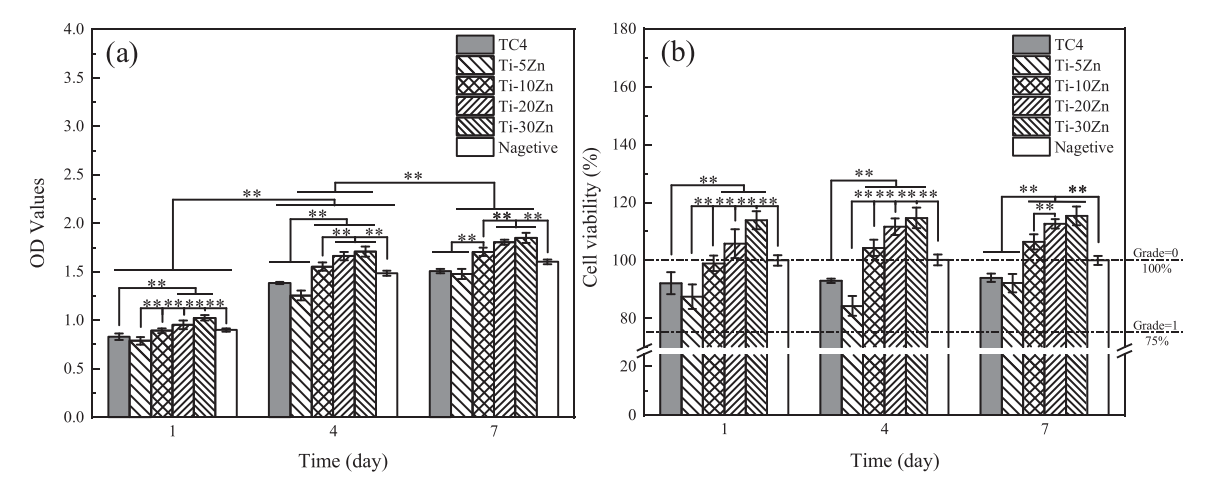


Fig. 14. OD values (a) and cell viabilities (b) of the MC3T3-E1 cells cultured on the surface of the Ti-Zn alloys for different times (** p < 0.01).

the Ti-Zn alloys are higher than 75% and ranked as more than Grade 1 for the biomedical materials, among which the cell viabilities of Ti-20Zn and Ti-30Zn alloys are higher than 100%, and can be ranked as Grade 0 for the biomedical materials. The Ti-Zn alloys have no cytotoxicity to the MC3T3-E1 cells and show the excellent ability to promote cell proliferation.

Fig. 15 shows the SEM images of the MC3T3-E1 cells cultured on the surface of the Ti-Zn alloys and TC4 alloy at 1 day and 7 days. A large number of cells are adhered to the surface of Ti-Zn alloys and TC4 alloy, and the number of cells increases with prolonging the culture times. After 1 day of culture, the cells adhered on the surface of the Ti-Zn alloys exhibit spindle-like or polygonal structure, indicating that the cells can adhere and spread well on the surface of Ti-Zn alloys. While the cells on the surface of the TC4 alloy are mostly spherical structures with a small amount of polygons, indicating that the spreading effect of cells on the surface of the TC4 alloy is worse than that on the surface of the Ti-Zn alloys. Moreover, the number of cells on the Ti-20Zn alloy is much higher than those on the Ti-5Zn alloy and TC4 alloy, which is greatly consistent with

the result of the OD values. When the culture time increases to 7 days, the surface of the Ti-20Zn alloy is completely covered by the cells, and the stratified proliferation of the cells also can be clearly observed. The surface of the Ti-5Zn alloy and TC4 alloy is not completely covered by the cells, and the serious agglomeration of the cells on the TC4 surface can be found. According to the abovementioned results, the Ti-20Zn alloy is more conducive to the adhesion, spreading and proliferation of MC3T3-E1 cells compared to the TC4 alloy, which is mainly attributed to the good hydrophilicity and the large amount of adsorbed OH on the surface of the Ti-20Zn alloy.

The ALP activities of the MC3T3-E1 cells cultured on the Ti-Zn alloys and TC4 alloy at 7 and 14 d are shown in Fig. 16. The ALP activity of the MC3T3-E1 cells cultured on the Ti-20Zn alloy displays significantly higher (p < 0.01) than those on the TC4 sample and other Ti-Zn alloys, and the ALP activities of the Ti-Zn alloys increase with prolonging the culture times. Generally, the ALP is a landmark enzyme in the early osteogenic differentiation of mature osteoblasts [73,74], and its activity indicates the activity and maturity of

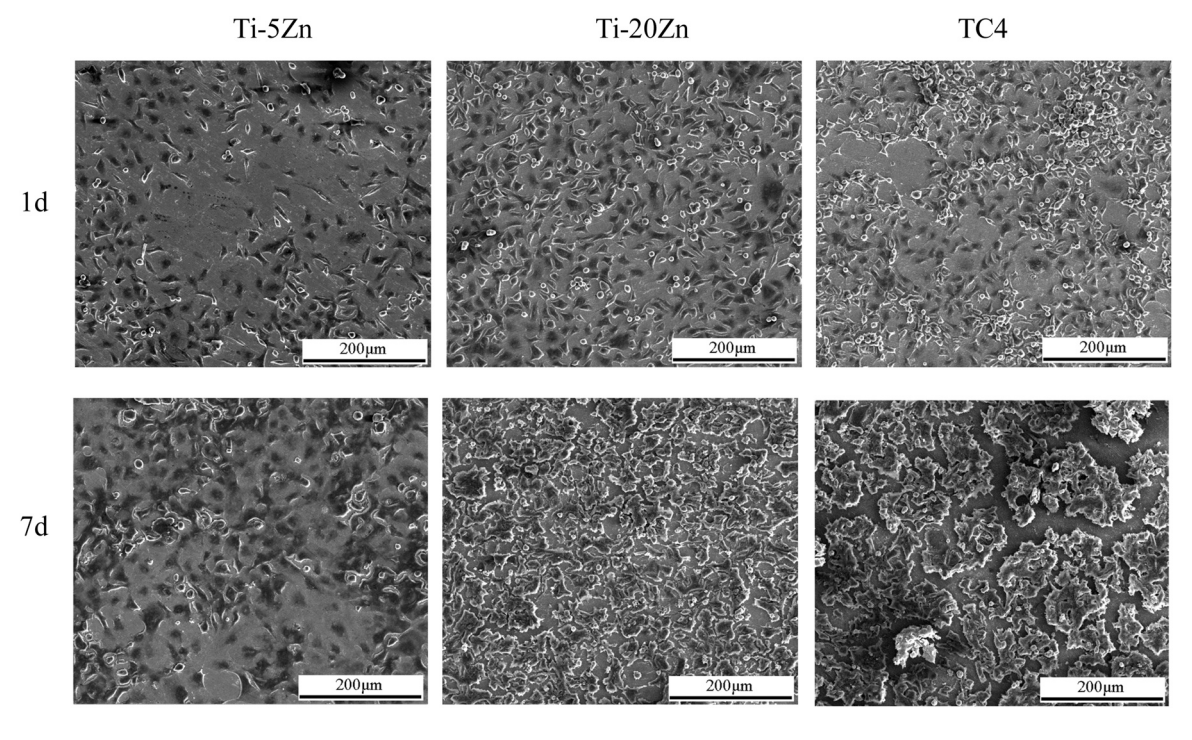


Fig. 15. SEM images of the MC3T3-E1 cells cultured on the surface of the Ti-Zn alloys and TC4 alloy at 1 day and 7 days.

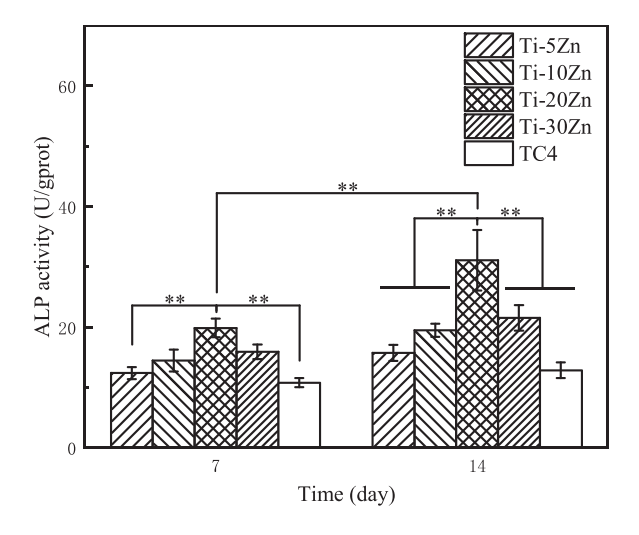


Fig. 16. ALP activities of the MC3T3-E1 cells cultured on the Ti-Zn alloys and TC4 at 7 and 14 days (** p < 0.01).

osteoblasts [75]. The ALP activity of the Ti-20Zn alloy indicates that the Ti-20Zn alloy can greatly promote the proliferation and differentiation of osteoblasts in the early stage of implantation in vivo and have good biological activity. The stable release of Zn ions from the Ti-20Zn alloy can inhibit the formation of osteoclasts in bone marrow cells, thus inhibiting the process of osteolysis [76] and improving osteoblast differentiation [77]. However, it is worth noting that the ALP activity of the MC3T3-E1 cultured on the Ti-30Zn alloys decreases compared to that of Ti-20Zn alloy, which may be attributed to the fact that higher concentration of Zn ions released from the Ti-30Zn alloy reduces the activity of osteoblasts and inhibits the proliferation and differentiation of osteoblasts [78,79]. Therefore, the proper release of Zn ions from the Ti-20Zn alloy can promote the proliferation of osteoblasts and enhance the expression of osteogenic genes, thus enhancing the differentiation of osteoblasts, improving the biological activity of the alloy, and improving the effectiveness of osteogenesis.

4. Conclusion

The novel biomedical Ti-Zn alloys were successfully fabricated by hot-press sintering. The microstructure, mechanical properties, corrosion resistance and in vitro biological properties of the Ti-Zn alloys were systematically evaluated. The following conclusions can be drawn:

- (1) The Ti-Zn alloys are mainly composed of α-Ti and Ti₂Zn phases. With increasing the Zn contents, the Ti₂Zn contents in the Ti-Zn alloys gradually increase. The existence of a large number of dislocations and Ti₂Zn secondary phase in Ti-Zn alloys can greatly enhance the strength and nanohardness of the alloys.
- (2) All of the compressive strength, elastic modulus, and nanohardness of the Ti-Zn alloys increase first, and then decrease with increasing the Zn contents. The elastic modulus is ranged from 17 GPa to 27 GPa, very close to that of the natural cortical bone.
- (3) The Ti-Zn alloys show excellent corrosion resistance in the SBF solution, and the Zn contents have no significant effect on the corrosion behavior. With increasing the immersion times, the corrosion resistance of Ti-20Zn alloy is continuously enhanced.
- (4) The Ti-Zn alloys exhibit good cytocompatibility, being beneficial to the spread, proliferation, and differentiation of the MC3T3-E1 cells. The release amount of Zn ions from the Ti-20Zn alloy is much lower than that of the biosafety intake. The Ti-20Zn alloy

exhibits excellent biological activity and is a promising biomedical material.

CRediT authorship contribution statement

M.H. Qi: Formal analysis; Investigation, Methodology, Visualization, Writing - review & editing, J.L. Xu: Conceptualization, Formal analysis, Funding acquisition, Investigation, Methodology, Writing - original draft, Writing - review & editing, T. Lai: Formal analysis; Investigation, Methodology, Writing - original draft, J. Huang: Methodology, Visualization, Writing - review & editing, Y.C. Ma: Methodology, Software, J.M. Luo: Formal analysis, Methodology, Y.F. Zheng: Conceptualization, Methodology.

Data Availability

Data will be made available on request.

Declaration of Competing Interest

The authors declare that they have no known competing financial interests or personal relationships that could have appeared to influence the work reported in this paper.

Acknowledgements

The authors gratefully acknowledge the financial support of the project from the National Natural Science Foundation of China (52161040), the Natural Science Foundation of Jiangxi Province, China (20202ACBL214011), and the Graduate Innovation Special Fund Project of Jiangxi Province (YC2022-s707).

References

- [1] M. Geetha, A.K. Singh, R. Asokamani, A.K. Gogia, Ti based biomaterials, the ultimate choice for orthopaedic implants-a review, Prog. Mater. Sci. 54 (2009)
- [2] L.C. Zhang, L.Y. Chen, A review on biomedical titanium alloys: recent progress and prospect, Adv. Eng. Mater. 21 (2019) 1801215.
 [3] S. Cao, Z.M. Zhang, J.Q. Zhang, R.X. Wang, X.Y. Wang, L. Yang, D.F. Chen, G.W. Qin,
- [3] S. Cao, Z.M. Zhang, J.Q. Zhang, R.X. Wang, X.Y. Wang, L. Yang, D.F. Chen, G.W. Qin, E.L. Zhang, Improvement in antibacterial ability and cell cytotoxicity of Ti-Cu alloy by anodic oxidation, Rare Met. 41 (2022) 594–609.
- alloy by anodic oxidation, Rare Met. 41 (2022) 594-609.

 [4] E. Zhang, X. Zhao, J. Hu, R. Wang, S. Fu, G. Qin, Antibacterial metals and alloys for potential biomedical implants, Bioact. Mater. 6 (2021) 2569-2612.
- [5] P.J. Denard, P. Raiss, R. Gobezie, T.B. Edwards, E. Lederman, Stress shielding of the humerus in press-fit anatomic shoulder arthroplasty: review and recommendations for evaluation, J. Shoulder Elb. Surg. 27 (2018) 1139–1147.
- [6] T. Terjesen, K. Apalset, The influence of different degrees of stiffness of fixation plates on experimental bone healing, J. Orthop. Res. 6 (1988) 293–299.
- [7] D.F. Williams, Biocompatibility pathways and mechanisms for bioactive materials: the bioactivity zone, Bioact. Mater. 10 (2022) 306–322.
 [8] N. Jiang, Z. Guo, D. Sun, Y. Li, Y. Yang, C. Chen, L. Zhang, S. Zhu, Promoting os-
- [8] N. Jiang, Z. Guo, D. Sun, Y. Li, Y. Yang, C. Chen, L. Zhang, S. Zhu, Promoting osseointegration of Ti implants through micro/nanoscaled hierarchical Ti phosphate/Ti oxide hybrid coating, ACS Nano 12 (2018) 7883–7891.
- [9] Y. Okazaki, S. Rao, S. Asao, T. Tateishi, S.-i Katsuda, Y. Furuki, Effects of Ti, Al and V concentrations on cell viability, Mater. Trans., JIM 39 (1998) 1053–1062.
 [10] Y. Okazaki, S. Rao, T. Tateishi, Y. Ito, Cytocompatibility of various metal and de-
- [10] Y. Okazaki, S. Rao, T. Tateishi, Y. Ito, Cytocompatibility of various metal and development of new titanium alloys for medical implants, Mater. Sci. Eng. A 243 (1998) 250–256.
- [11] M.Z. Ibrahim, A.A. Sarhan, F. Yusuf, M. Hamdi, Biomedical materials and techniques to improve the tribological, mechanical and biomedical properties of orthopedic implants—A review article, J. Alloy. Compd. 714 (2017) 636–667.
- [12] L.J. Xu, S.L. Xiao, J. Tian, Y.Y. Chen, Y.D. Huang, Microstructure and dry wear properties of Ti-Nb alloys for dental prostheses, Trans. Nonferrous Met. Soc. China 19 (2009) S639–S644.
- [13] X.F. Zhao, M. Niinomi, M. Nakai, J. Hieda, Beta type Ti-Mo alloys with changeable Young's modulus for spinal fixation applications, Acta Biomater. 8 (2012) 1990–1997.
- [14] P.F. Santos, M. Niinomi, K. Cho, M. Nakai, H.H. Liu, N. Ohtsu, M. Hirano, M. Ikeda, T. Narushima, Microstructures, mechanical properties and cytotoxicity of low cost beta Ti-Mn alloys for biomedical applications, Acta Biomater. 26 (2015) 366–376
- [15] J.Z. Niu, Y.H. Guo, K. Li, W.J. Liu, Z.H. Dan, Z.G. Sun, H. Chang, L. Zhou, Improved mechanical, bio-corrosion properties and in vitro cell responses of Ti-Fe alloys as candidate dental implants, Mater. Sci. Eng. C 122 (2021) 111917.
- [16] E.L. Zhang, X.Y. Wang, M. Chen, B. Hou, Effect of the existing form of Cu element on the mechanical properties, bio-corrosion and antibacterial properties of Ti-Cu alloys for biomedical application, Mater. Sci. Eng. C 69 (2016) 1210–1221.

- [17] T. Lai, J.L. Xu, J. Huang, Q. Wang, J.P. Zhang, J.M. Luo, Partially biodegradable Ti-Mg composites prepared by microwave sintering for biomedical application, Mater. Charact. 185 (2022) 111748.
- [18] H. Li, K. Qiu, W. Yuan, F. Zhou, B. Wang, L. Li, Y. Zheng, Y. Liu, Screening on binary Ti alloy with excellent mechanical property and castability for dental prosthesis application, Sci. Rep. 6 (2016) 1–10.
- [19] X. Liu, S. Chen, J.K. Tsoi, J.P. Matinlinna, Binary titanium alloys as dental implant materials—a review, Regen. Biomater. 4 (2017) 315–323.
 [20] E. Mostaed, M. Sikora-Jasinska, J.W. Drelich, M. Vedani, Zinc-based alloys for
- egradable vascular stent applications. Acta Biomater. 71 (2018) 1–23.
- [21] X. Liu, H.T. Yang, P. Xiong, W.T. Li, E.H. Huang, Y.F. Zheng, Comparative studies of Tris-HCl, HEPES and NaHCO₃/CO₂ buffer systems on the biodegradation behaviour of pure Zn in NaCl and SBF solutions, Corros. Sci. 157 (2019) 205–219.
- [22] P.K. Bowen, J. Drelich, J. Goldman, Zinc exhibits ideal physiological corrosion
- behavior for bioabsorbable stents, Adv. Mater. 25 (2013) 2577–2582.

 [23] H. Yang, C. Wang, C. Liu, H. Chen, Y. Wu, J. Han, Z. Jia, W. Lin, D. Zhang, W. Li, W. Yuan, H. Guo, H. Li, G. Yang, D. Kong, D. Zhu, K. Takashima, L. Ruan, J. Nie, X. Li, Y. Zheng, Evolution of the degradation mechanism of pure zinc stent in the onerear study of rabbit abdominal aorta model, Biomaterials 145 (2017) 92–105.
- [24] H. Guo, R.H. Cao, Y.F. Zheng, J. Bai, F. Xue, C.L. Chu, Diameter-dependent in vitro performance of biodegradable pure zinc wires for suture application, J. Mater.
- Sci. Technol. 35 (2019) 1662–1670.

 [25] H. Guo, D. Xia, Y. Zheng, Y. Zhu, Y. Liu, Y. Zhou, A pure zinc membrane with degradability and osteogenesis promotion for guided bone regeneration: In vitro and in vivo studies, Acta Biomater. 106 (2020) 396–409.
- [26] B. Jia, Z. Zhang, Y. Zhuang, H. Yang, Y. Han, Q. Wu, X. Jia, Y. Yin, X. Qu, Y. Zheng, K. Dai, High-strength biodegradable zinc alloy implants with antibacterial and osteogenic properties for the treatment of MRSA-induced rat osteomyelitis, Biomaterials 287 (2022) 121663.
- [27] D. Zhu, I. Cockerill, Y. Su, Z. Zhang, J. Fu, K.-W. Lee, J. Ma, C. Okpokwasili, L. Tang, Y. Zheng, Mechanical strength, biodegradation, and in vitro and in vivo bio-compatibility of Zn biomaterials, ACS Appl. Mater. Interfaces 11 (2019) 6809-6819
- [28] X. Tong, D. Zhang, X. Zhang, Y. Su, Z. Shi, K. Wang, J. Lin, Y. Li, J. Lin, C. Wen, Microstructure, mechanical properties, biocompatibility, and in vitro corrosion and degradation behavior of a new Zn-5Ge alloy for biodegradable implant materials, Acta Biomater. 82 (2018) 197–204.
- [29] H. Hermawan, Updates on the research and development of absorbable metals
- for biomedical applications, Prog. Biomater. 7 (2018) 93–110.

 [30] D.A. Brice, P. Samimi, I. Ghamarian, Y. Liu, M.Y. Mendoza, M.J. Kenney, R.F. Reidy, M. Garcia-Avila, P.C. Collins, On the eutectoid transformation behavior of the Ti-Zn system and its metastable phases, J. Alloy. Compd. 718 (2017) 22–27.
- [31] D. Gordin, R. Ion, C. Vasilescu, S. Drob, A. Cimpean, T. Gloriant, Potentiality of the Gum Metal" titanium-based alloy for biomedical applications, Mater. Sci. Eng. C 44 (2014) 362-370.
- [32] Q. Wei, L. Wang, Y. Fu, J. Qin, W. Lu, D. Zhang, Influence of oxygen content on microstructure and mechanical properties of Ti-Nb-Ta-Zr alloy, Mater. Des. 32 (2011) 2934-2939
- [33] A. Robin, O. Carvalho, S. Schneider, S. Schneider, Corrosion behavior of Ti-xNb-13Zr alloys in Ringer's solution, Mater. Corros. 59 (2008) 929–933.
- [34] X. San, X. Liang, L. Chen, Z. Xia, X. Zhu, Influence of stacking fault energy on the mechanical properties in cold-rolling Cu and Cu-Ge alloys, Mater. Sci. Eng. A 528 2011) 7867
- [35] ASTM-E111-97. American Society for testing and materials, Philadelphia, PA, USA, 2004.
- [36] International Organization for Standardization. Metallic Materials: Instrumented Indentation Test for Hardness and Materials Parameters, Test Method [M], ISO,
- [37] J.L. Xu, J.L. Zhang, L.Z. Bao, T. Lai, J.M. Luo, Y.F. Zheng, Preparation and bioactive surface modification of the microwave sintered porous Ti-15Mo alloys for biomedical application, Sci. China Mater. 61 (2018) 545-556.
- [38] H. Okamoto, Ti-Zn (titanium-zinc), J. Ph. Equilib. Diffus. 29 (2008) 211-212.
- C.R. Hubbard, R.L. Snyder, RIR-measurement and use in quantitative XRD, Powder Diffr. 2 (1988) 74–77.
- [40] J.L. Xu, S.C. Tao, L.Z. Bao, J.M. Luo, Y.F. Zheng, Effects of Mo contents on the microstructure, properties and cytocompatibility of the microwave sintered porous Ti-Mo alloys, Mater. Sci. Eng. C 97 (2019) 156-165.
- J. Xing, Z. Xia, J. Hu, Y. Zhang, L. Zhong, Time dependence of growth and crysallization of anodic titanium oxide films in potentiostatic mode, Corros. Sci. 75 2013) 212-219.
- [42] E. Milella, F. Cosentino, A. Licciulli, C. Massaro, Preparation and characterisation of titania/hydroxyapatite composite coatings obtained by sol-gel process, Biomaterials 22 (2001) 1425–1431.
- [43] J.F. Moulder, W.F. Stickle, P.E. Sobol, K.D. Bomben, Handbook of X-Ray Photoelectron Spectroscopy, Perkin-Elmer Corp, Eden Práire, MN, 1992.
- [44] K. Sahu, A. Bisht, S. Kuriakose, S. Mohapatra, Two-dimensional CuO-ZnO nanohybrids with enhanced photocatalytic performance for removal of pollutants, J. Phys. Chem. Solids 137 (2020) 109223.
- [45] J. Silvestre-Albero, F. Coloma, A. Sepúlveda-Escribano, F. Rodríguez-Reinoso, Effect of the presence of chlorine in bimetallic PtZn/CeO₂ catalysts for the vaporphase hydrogenation of crotonaldehyde, Appl. Catal. A Gen. 304 (2006) 159–167.
- [46] J. Fox, J. Nuttall, T. Gallon, Solid state effects in the Auger spectrum of zinc and oxidised zinc, Surf. Sci. 63 (1977) 390-402.
- [47] M.N. Islam, T. Ghosh, K. Chopra, H. Acharya, XPS and X-ray diffraction studies of aluminum-doped zinc oxide transparent conducting films, Thin Solid Films 280 1996) 20-25.
- Y. Yang, S. Wu, G. Li, Y. Li, Y. Lu, K. Yang, P. Ge, Evolution of deformation mechanisms of Ti-22.4Nb-0.73Ta-2Zr-1.34O alloy during straining, Acta Mater. 58 (2010) 2778-2787.

- [49] Y. Rho, R.B. Ashman, C.H. Turner, Young's modulus of trabecular and cortical bone material: ultrasonic and microtensile measurements, J. Biomech. 26 (1993) 111_119
- [50] B. Yuan, J. Du, X. Zhang, Q. Chen, Y. Wan, Z. Xing, H. Zhan, Microstructures and room-temperature compressive properties of Ti6Al4V alloy processed by continuous multistep hydrogenation treatment, Int. J. Hydrog. Energy 45 (2020) 25567-25579
- [51] S. Guo, Q. Meng, X. Zhao, Q. Wei, H. Xu, Design and fabrication of a metastable βtype titanium alloy with ultralow elastic modulus and high strength, Sci. Rep. 5 (2015) 1-8
- [52] Y.L. Zhou, M. Niinomi, T. Akahori, Decomposition of martensite α" during aging treatments and resulting mechanical properties of Ti-Ta alloys, Mater. Sci. Eng. A 384 (2004) 92-101.
- [53] H. Rack, J. Qazi, Titanium alloys for biomedical applications, Mater. Sci. Eng. C 26 2006) 1269-1277.
- M. Bermingham, T. Li, J. Cooper-White, M.S. Dargusch, Sintering and biocompatibility of blended elemental Ti-xNb alloys, J. Mech. Behav. Biomed. Mater. 104 (2020) 103691.
- [55] M. Niinomi, Mechanical properties of biomedical titanium alloys, Mater. Sci. Eng. A 243 (1998) 231-236.
- [56] C. Yi, Z. Ke, L. Zhang, J. Tan, Y. Jiang, Z. He, Antibacterial Ti-Cu alloy with enhanced mechanical properties as implant applications, Mater. Res. Express 7 2020) 105404.
- [57] M.F. Doerner, W.D. Nix, A method for interpreting the data from depth-sensing indentation instruments, J. Mater. Res. 1 (1986) 601–609.

 [58] H.F. Li, J.Y. Huang, G.C. Lin, P.Y. Wang, Recent advances in tribological and wear
- properties of biomedical metallic materials, Rare Met. 40 (2021) 3091-3106.
- [59] P.P. Socorro-Perdomo, N.R. Florido-Suárez, J.C. Mirza-Rosca, M.V. Saceleanu, EIS characterization of Ti alloys in relation to alloying additions of Ta, Materials 15 (2022)476.
- [60] M.R. Akbarpour, H.M. Mirabad, A. Hemmati, H.S. Kim, Processing and microstructure of Ti-Cu binary alloys: a comprehensive review, Prog. Mater. Sci. (2022) 100933.
- [61] J.L. Xu, F. Liu, F.P. Wang, D.Z. Yu, L.C. Zhao, The corrosion resistance behavior of Al₂O₃ coating prepared on NiTi alloy by micro-arc oxidation, J. Alloy. Coumpd. 472 (2009) 276–280.
- [62] M. Qi, B. Chen, C. Xia, Y. Liu, S. Liu, H. Zhong, X. Zou, T. Yang, Q. Li, Microstructure, mechanical properties and biocompatibility of novel Ti-20Zr-xMo alloys, J. Alloy. Compd. 888 (2021) 161478.
- [63] R. Prasannakumar, V. Chukwuike, K. Bhakyaraj, S. Mohan, R. Barik, Electrochemical and hydrodynamic flow characterization of corrosion protection persistence of nickel/multiwalled carbon nanotubes composite coating, Appl. Surf. Sci. 507 (2020) 145073.
- [64] I. Caha, A. Alves, P. Kuroda, C. Grandini, A. Pinto, L. Rocha, F. Toptan, Degradation behavior of Ti-Nb alloys: Corrosion behavior through 21 days of immersion and tribocorrosion behavior against alumina, Corros. Sci. 167 (2020) 108488.
- [65] E.M. Harnett, J. Alderman, T. Wood, The surface energy of various biomaterials coated with adhesion molecules used in cell culture, Coll. Surf. B Biointerfaces 55 (2007) 90-97
- [66] S. Fu, X. Zhao, L. Yang, G. Qin, E. Zhang, A novel Ti-Au alloy with strong antibacterial properties and excellent biocompatibility for biomedical application, Biomater. Adv. 133 (2022) 112653.
- [67] L. Liang, Q. Huang, H. Wu, Z. Ouyang, T. Liu, H. He, J. Xiao, G. Lei, K. Zhou, Stimulation of in vitro and in vivo osteogenesis by Ti-Mg alloys with the sustained-release function of magnesium ions, Coll, Surf. B Biointerfaces 197 (2021) 111360
- [68] Z. Li, H. Xu, A. Dong, J. Qiu, L. He, T. Zhang, D. Du, H. Xing, G. Zhu, D. Wang, B. Sun, Characteristics of Ti-Nb-Mg alloy by powder metallurgy for biomedical applications, Mater. Charact. 173 (2021) 110953.
- G.J. Fosmire, Zinc toxicity, Am. J. Clin. Nutr. 51 (1990) 225–227. C. Ning, X. Wang, L. Li, Y. Zhu, M. Li, P. Yu, L. Zhou, Z. Zhou, J. Chen, G. Tan, Y. Zhang, Y. Wang, C. Mao, Concentration ranges of antibacterial cations for showing the highest antibacterial efficacy but the least cytotoxicity against mammalian cells: implications for a new antibacterial mechanism, Chem. Res. Toxicol. 28 (2015) 1815-1822.
- [71] J. Luo, S. Guo, Y. Lu, X. Xu, C. Zhao, S. Wu, J. Lin, Cytocompatibility of Cu-bearing Ti6Al4V alloys manufactured by selective laser melting, Mater. Charact. 143 (2018) 127-136.
- [72] R. Liu, K. Memarzadeh, B. Chang, Y. Zhang, Z. Ma, R.P. Allaker, L. Ren, K. Yang, Antibacterial effect of copper-bearing titanium alloy (Ti-Cu) against Streptococcus mutans and Porphyromonas gingivalis, Sci. Rep. 6 (2016) 29985.
- [73] E.E. Golub, K. Boesze-Battaglia, The role of alkaline phosphatase in mineralization, Curr. Opin. Orthop. 18 (2007) 444–448.
- [74] M. Simann, V. Schneider, S. Le Blanc, et al., Heparin affects human bone marrow stromal cell fate: Promoting osteogenic and reducing adipogenic differentiation and conversion, Bone 78 (2015) 102–113.
- [75] J.B. Lian, G.S. Stein, Concepts of osteoblast growth and differentiation: basis for modulation of bone cell development and tissue formation, Crit. Rev. Oral. Biol. Med. 3 (1992) 269-305.
- [76] M. Yamaguchi, Role of zinc in bone formation and bone resorption, J. Trace Elem. Exp. Med. 11 (1998) 119-135.
- [77] Y. Qiao, W. Zhang, P. Tian, et al., Stimulation of bone growth following zinc incorporation into biomaterials, Biomaterials 35 (2014) 6882-6897.
- J. Ma, N. Zhao, D. Zhu, Bioabsorbable zinc ion induced biphasic cellular responses in vascular smooth muscle cells, Sci. Rep. 6 (2016) 1–10. [79] J. Ma, N. Zhao, D. Zhu, Endothelial cellular responses to biodegradable metal
- zinc, ACS Biomater. Sci. Eng. 1 (2015) 1174-1182.